Accepted for publication in Journal of Composite Structures - 14/12/2020

Numerical analysis of high velocity, oblique impacts and residual tensile strength of carbon/epoxy laminates

Ashwin R Kristnama, Xiaodong Xu, Michael R Wisnom, Stephen R Hallett*

Bristol Composites Institute (ACCIS), University of Bristol, University Walk, Bristol BS8 1TR, UK.

Abstract

This paper presents prediction of the high velocity, oblique impact response and quasi-static residual tensile strength of thin $[45/90/-45/\ 0]_{2s}$ carbon/epoxy laminates using finite element (FE) models. A High-Fidelity Finite Element Method (Hi-FEM) with an automated unit cell meshing technique was employed. The predicted impact damage, characterised by the extent of fibre failure and delamination area, was validated against results from gas-gun tests for a range of impact velocities. The numerical results captured the trend of increasing impact damage with impact energy as observed from the tests. Changes in projectile orientation before impact were shown to increase the extent of fibre failure at high impact energies, up by 38% in edge impact cases. The residual tensile strength of the impacted laminates was then investigated, where the numerical results for edge-impacted laminates agreed with the test data within 8%. On the other hand, the residual strength modelling results of centre-impacted laminates were found to be unconservative, mainly due to the extent of fibre failure predicted during impact. Machined notches were also studied for their residual tensile strength in comparison to impact induced damage. The predicted strength of edge-notched laminates was found to be in close agreement with the experimental results for edge-impacted laminates, differing by an average of 9%.

Keywords: Laminate, Impact behaviour, Strength, Finite element analysis (FEA), Notch

1. Introduction

The aerospace industry has been very active in reducing fuel consumption over the years. To this end, the two main strategies considered are reductions in structural weight and increasingly efficient engines. The Airbus A350 and Boeing 787 use around 50% of composite materials and in this context, the structural problem of high velocity impact due to foreign object damage on aircraft components made from composite materials has become a subject of great interest. In the early 90's, Abrate [1] presented a comprehensive view of the state of art in impact on composite structures with focus on low velocity impact. Cantwell and Morton [2] identified fundamental parameters, such as fibre and matrix properties, target geometry and loading rate, which determine the impact resistance of continuous fibre-reinforced composites. In the following decades, there has been an increasing demand for advanced and

*Corresponding author
Email-address: akristnama7@gmail.com (Kristnama AR)

robust numerical models for virtual testing which are capable of accurately capturing the failure modes with high fidelity and computational efficiency [3,4].

Several Finite Element (FE) modelling techniques have been proposed to predict impact damage in laminated composites. *Ebina et al.* [5] presented a hi-fidelity FE model to capture the low velocity impact response of 4.71 mm thick IMS60/133 laminates at an impact energy of 31.6 J. A smeared crack model (SCM) was used to model fibre damage. In-plane ply cracks were modelled using an enhanced continuum damage mechanics (ECDM) model, which consisted of continuum damage mechanics (CDM) and SCM. Cohesive behaviour based on a contact formulation was employed to model delamination between plies. The model under-predicted the delamination areas and no delamination was observed in the lower interfaces opposite the impacted side. The authors attributed these limitations to the lack of definition of the interaction between matrix cracks and delamination. *Cui et al.* [6] predicted impact damage in 5 mm thick IM7/8552 composite plates for a range of velocities between 21 - 157 m/s, where the Puck [7] and LaRC [8] failure criteria were implemented for the inter-fibre failure damage and delamination. The LaRC-based model over-predicted the extent of damage while the damage was under-predicted in the Puck-based model for velocities close to the ballistic limit. Numerical instabilities due to element distortion and failure were also reported. *Pernas-Sanchez et al.* [9] developed a numerical methodology to predict the impact damage on unidirectional laminates using a steel sphere of 7.5 mm diameter. Inter- and intra- laminar failures were modelled through a cohesive interaction and stress-based damage criterion respectively, including fibre failure under tension and compression, matrix failure under compression and tension. The model was successfully validated against experimental data in terms of residual velocity and the trend in delaminated area. Nonetheless, some differences were observed between the numerical and experimental delaminated area. As delamination spreads via matrix cracks, the stress-based failure criterion for matrix failure is not enough to capture the matrix damage propagation.

Cohesive zone models (CZM) are one of the major approaches to describe matrix crack and delamination growth while satisfying mesh objectivity [10,11]. One of the drawbacks is the necessity of using pre-defined crack paths when using cohesive elements for describing matrix

cracks. While investigating size effects in centre-notched laminates, *Xu et al.* [12] employed a two-parameter integrated Weibull model combined with cohesive interface elements, for progressive tensile fibre failure in composite laminates [13]. Multiple potential split paths were pre-defined in the plies to simulate the damage zone at the notch tips. The authors found good correlation between experimental and numerical results, where delamination shapes, split lengths and scaling of the damage zone were a function of notch size. In a more recent study, *Xu et al.* [14] developed a Hi-Fidelity Finite Element Method (Hi-FEM) to predict the Mode I trans-laminar fracture toughness in composite laminates. The Hi-FEM combines the Weibull fibre failure criterion with potential delamination and multiple split paths modelled using cohesive elements, together with an automated meshing technique developed by *Li et al.* [15]. The unit cell meshing technique is advantageous as it can accommodate potential splitting of different orientations. The application of the Weibull theory for tensile fibre failure alongside the unit cell meshing technique under impact scenarios has not previously been investigated.

Generally, the damage area due to impact extends to a significantly larger area than is visible from the surface and can severely reduce the load-bearing capability. The ASTM compression after impact (CAI) test is a standardised strength measurement [16-18], but tension after impact can be equally important for structural components that are subject to high centrifugal forces. *Koo et al.* [19] predicted the residual strength of low velocity impacted composite structures by using a characteristic length, with the hole diameter corresponding to the impact damage area. The predicted results using the corresponding hole diameter showed good agreement with experimental results. Modelling impact damage initiation and its progression under load can be particularly expensive in the preliminary design phase. Consequently, simplified damage models using machined notches as a proxy for impact damage can avoid the high costs associated with intensive computational analysis. While several studies have compared the compressive strength of impacted laminates to laminates with a circular hole [20-22] or an elliptical hole [23], this study aims to assess machined notches as a potential equivalent for tension after impact tests by comparing the damage development between impacted and machined notch laminates.

In a previous study, the authors conducted an experimental investigation of high velocity oblique impact and residual tensile strength of carbon/epoxy laminates [24]. In the current study, the Hi-FEM employed takes a new approach to model these high velocity impacts whilst addressing the limitation found in the open literature linked to the interactions between matrix cracks and delamination. The fibre failure due to tension is modelled using a stress criterion based on Weibull theory, the compressive fibre failure is modelled based on a maximum stress criterion and an automated unit cell meshing technique is employed to model detailed damage patterns including multiple split paths and delamination using cohesive interface elements. The numerical impact results are validated against the experimental data. The residual tensile strength of impacted laminates is then predicted and compared against experimental results. The current study further investigates and compares the residual tensile strength results with those from machined notches.

2. Numerical Model

A Hi-FEM is employed in this numerical study, which combines different failure criteria with multiple split paths and delamination modelled using cohesive interface elements. An automated unit cell meshing technique is utilised and the numerical methodology was implemented in LS-DYNA.

2.1. Impactor

In the experiments, a 3 mm steel cube projectile was used to impact target laminates at their edge and centre, at a 45° incident angle. Due to negligible deformation observed from recovered projectiles, plastic deformation of the projectile is not considered. Hence, the steel cube projectile is assumed linear-elastic and is modelled using the following properties: density (ρ) = 7850 kg/m^3, Young's modulus (E_{steel}) = 210 GPa and Poisson's ratio (ν) = 0.3.

2.2. In-plane failure

The plies follow the behaviour of an orthotropic elastic material until failure, with Hexcel's IM7/8552 carbon-fibre/epoxy pre-preg system's properties given in *Table 1*. Fibre tensile failure is predicted using the Weibull theory, which is based on a weakest-link principle

[13]. The strength of a brittle-like material is assumed to be related to the stressed volume and controlled by defects that follow a Weibull distribution [25]. Assuming equal probability of survival between the model and a unit volume of material, fibre failure occurs when *Equation (1)* is met.

$$\int_V \left(\frac{\sigma}{\sigma_{unit}}\right)^m dV = \sum_{i=1}^{TotalNo.ofsolidElements} \left(\frac{\sigma_i}{\sigma_{unit}}\right)^m V_i = 1 \quad (1)$$

where σ_i is the stress in element *i*, V_i is the volume of element *i*, σ_{unit} is the tensile strength of a unit volume of material and m is the Weibull modulus, measured from scaled unnotched unidirectional tensile tests of the same material [26]. For 1 mm^3 of material, we can derive the constants as m = 41 and σ_{unit} = 3131 MPa. *Equation (1)* is checked at each time step. When this criterion is satisfied, the element with maximum fibre direction stress is removed and load redistribution to the remaining elements occurs. As the applied load is increased, the stresses in the remaining elements build up until *Equation (1)* is satisfied again. Then, the next element with maximum fibre direction stress is deleted. This represents the continuous fibre breakage process during the damage zone development [12,27] and fracture propagation [14].

The fibre failure criterion under compression is given by *Equation (2).* When the parameter associated with the failure criteria $e_{f,c}^2$ is equal to zero, the elements are removed from the calculations.

$$e_{f,c}^2 = \left(\frac{\sigma_{11}}{X_C}\right)^2 - 1 \quad (2)$$

where X_C = 1690 MPa is the strength of the laminate in the fibre direction under compression, as provided by the manufacturer [28].

2.3. Inter-laminar failure

A cohesive formulation developed by *Jiang et al*. [29] is adopted here and implemented into the non-linear explicit solver, LS-DYNA, via a user-material subroutine. The

cohesive formulation is governed by a bi-linear traction-separation law (TSL), as shown in *Figure 1,* which relates the traction and separation of the cohesive element under mixed-mode loading, with the area under the bi-linear curve being the critical Energy Release Rate (ERR). When the critical ERR is reached, the failed cohesive interface elements are deleted. The cohesive formulation also considers the enhancement effect of through-thickness compression on shear behaviour through a material-dependent factor to correctly capture the Mode II behaviour [30]. The enhancement factor is critical in controlling the load corresponding to the delamination initiation, where it serves as an internal friction coefficient that increases the shear strength and Mode II critical energy release rate in the presence of through-thickness compressive stress. The rate dependent failure envelope of IM7/8552 found in [6], shows there is not a strong high-rate dependency. As such, the cohesive properties used for IM7/8552, as listed in *Table 2* [12,31,32] are constant values taken from dynamic tests.

2.4. Finite element model

Each ply out of the 16-ply carbon/epoxy laminate used in the impact tests was modelled as a single layer of constant-stress reduced integration 8-noded brick elements (Type-1 in LS-DYNA) with stiffness-based hourglass control. 8-noded zero-thickness cohesive elements (Type-19 in LS-DYNA) were employed to represent the thin resin layers between plies where delamination may arise. In addition, cohesive elements were also utilised to model multiple pre-defined potential split paths parallel to the fibres within the plies.

The impact configurations are taken from reference [24] and shown in *Figure 2,* where impacts were carried out close to the edge and away from the edge to investigate the extent of impact damage due to the oblique trajectory of the projectile. To reproduce the experimental boundary conditions, all the nodes through the thickness over a length of 40 mm from the end where the specimens were clamped were selected and given Single Point Constraint (SPC) boundary conditions in LS-DYNA. This is represented in *Figure 3*, which also shows the orientation of the projectile before impact. A Region of Interest (RoI) was defined for the laminate with an average mesh size of 0.23 mm. A typical FE mesh within the RoI which is based on a unit cell [15] is illustrated in *Figure 3*. By inputting the unit cell mesh size, dimension

of each ply, stacking sequences and spacing of pre-defined split paths in the plies, an automated meshing tool generates the basic mesh for each oriented ply. Cohesive elements for inter-laminar failure are inserted between every ply and cohesive elements for intra-ply splits are inserted at interfaces between different areas. The 0°, 90°, 45° and -45° splits based on a unit cell pattern are depicted in *Figure 4*. There is a minimum allowable split spacing where 0° and 90° splits are 0.71 mm apart and the oblique splits are 1 mm apart. Further reductions in split spacing would require smaller mesh sizes, hence higher computational costs, but were not necessary as *Xu et al*. [12] reported that 1 mm spacing is sufficient for tensile strength predictions.

A thermal load of -160 °C was included in the simulations prior to the impact loading, to model the generation of thermal residual stresses due to cooling down of the laminate from the 180 °C cure temperature to room temperature after the autoclave process. In LS-DYNA, a thermal load curve is defined with thermal expansion coefficients for IM7/8552 provided in *Table 1* [12]. The nodal temperatures are the same throughout the model and vary according to the load curve, where the temperature is defined as a function of time. Eroding surface-to-surface contact was defined between the laminate and the projectile. An additional automatic surface-to-surface contact was defined between each ply to limit the extent to which solid elements interpenetrate each other after cohesive elements are deleted. Frictional effects between the projectile and target were considered based on a basic Coulomb friction model, which is defined by two contacting surfaces carrying shear stresses up to a critical value that is dependent on the contact pressure. The coefficient of friction was set to a value of 0.3 for the steel/composite contact [33].

3. High velocity impact tests

Using a gas gun, high velocity impacts were carried out at 45° to the edge and centre of the laminates over a range of velocities between 100 m/s and 350 m/s, at intervals of 50 m/s, as described in [24]. The material used was Hexcel HexPly® IM7/8552 carbon-epoxy pre-preg with a nominal ply thickness of 0.125 mm. All laminates were cut into rectangular specimens of 250 mm length and 40 mm width, with a quasi-isotropic stacking sequence $[45/90/-45/\ 0]_{2s}$.

Two impact damage characteristics were considered to assess the reliability of the impact model, namely the extent of fibre failure and the size of the delamination area. Both were quantified using X-Ray Computed Tomography (CT) and the ImageJ® software, with detailed experimental results presented in [24]. The extent of fibre fracture for all impact configurations, termed as fibre fracture width, was characterised by measuring the widths of broken fibres for all broken plies and averaging over the number of plies showing fibre failure. The delamination area was characterised by measuring the area at any delaminated interfaces and averaging over the number of delaminated interfaces.

4. High velocity impact simulation

The set of high velocity impact configurations, as illustrated in *Figure 2*, has been simulated in LS-DYNA for a duration of 0.5 ms over a range of velocities. Typical runtimes for the simulations vary from 10 hours of analysis time for lower velocities to 48 hours for higher velocities on a high performance computer cluster. At the end of each analysis, the hourglass energy was computed and found to be approximately 5% of the system internal energy, which is considered acceptable.

The test vs FE fibre fracture widths versus impact energy are presented in *Figure 5* and *6* for edge and centre impacts respectively. For both impact configurations, the trends are captured for the extent of fibre failure increasing with greater impact energy. Large variations are observed in the fibre fracture widths for a given impact energy as shown by the error bars, which are due to a much greater extent of fibre failure in the plies close to the impact point than in the plies away from the impact point. For edge impacts, the predicted fibre fracture widths differ from the experimental results by an average of 26%. For centre impacts beyond 1.1 J, the predicted fibre fracture widths fluctuate from the experimental data by an average difference of 30%. These differences observed in the predicted and actual fibre fracture widths are believed to be due to possible variations in the orientation of the projectile before impact and the fact that there might be a slight variation in exactly where the projectile strikes the laminate. While the latter has not been considered in this work, a sensitivity analysis needs to be carried out to validate this argument.

The variations in delamination area with impact energy are depicted in *Figures 7* and *8* for edge and centre impacts respectively. Also shown in *Figures 7* and *8* are the error bars associated with the variations in delamination area of the individual interfaces from the mean in a single specimen. For edge impacts, the predicted delamination area increases with impact energy and beyond 9.9 J, the area increases more slowly. In the edge impact tests, laminate perforation was observed at 9.9 J and was accompanied by a maximum delamination area. The impact model fails to predict laminate perforation at 9.9 J. The delamination areas are correctly predicted at lower impact energies for centre impacts, yet, the predicted delamination areas lie well below the experimental results when the impact energy is increased beyond 6.5 J.

The differences between predicted and actual delamination areas may be linked to the number and position of interface layers which were shown to significantly influence the delamination patterns [33]. In addition, the impact model consists of only one element per ply in the through thickness direction, and upon initiation of delamination, individual plies using elements with reduced integration lose their bending stiffness. As the extent of delamination propagating during an impact event is dependent on the laminate's residual bending stiffness, the impact model does not capture the correct delamination areas for some impact energies.

In this study, delamination area has been characterised as an average value of all delaminated interfaces. Nevertheless, the total delamination area and the projected delamination area were also considered. However, neither total delamination area nor projected delamination area yielded closer predictions to the experimental results.

4.2. Effect of projectile orientation

This section investigates the influence of different projectile orientations before impact at 13.5 J on the extent of impact damage. The baseline orientation of the projectile, shown in *Figure 3*, relates to the flat face of the projectile impacting the target. The first variation in the projectile's orientation considered is where the edge of the projectile strikes the target and is referred to as 'edge'. The second one relates to the projectile striking the target in a 'point first' configuration, which is referred to as 'point'. As before, an oblique impact is simulated with the

projectile striking the target at 1.5 mm and 20 mm from the edge. The influence of the projectile's orientation on the extent of fibre failure and delamination area is presented in *Figures 9* and *10* respectively. The error bars in *Figures 9* and *10* are associated with the variations in impact damage in a single specimen. The fibre fracture width increases as the contact area between the projectile and target decreases, where the 'point' configuration in edge and centre impacts shows on average a 60% increase compared to the baseline. For edge and centre impacts, an increase of 3% in the delamination area is observed when the contact area is decreased from the baseline configuration to the 'edge' configuration. As the contact area is further decreased, the delamination areas are significantly larger than the baseline. It is notable that the experimental fibre fracture widths which lie within the range of predicted fibre fracture widths with different orientations.

5. Residual tensile strength

This section describes the finite element model used for tensile strength predictions with initial damage obtained from the impact models and assesses the predictions in comparison to the experimental results [24]. While the residual tensile strength is mainly governed by the extent of fibre fracture, it is also desirable to examine the relationship between the residual strength and the length of 0° splits, which is why the propagation of initial 0° splits in impacted and notched laminates are investigated.

5.1. Finite element model

The laminate model, cohesive formulation and fibre failure criterion under tension using the Weibull theory have been previously explained in section 2 of this paper for the impact models, and pertinent information is not repeated except for the description of some key features of the tensile simulations. After the impact simulation, a keyword file was written in LS-DYNA after the damage had fully formed and all failed elements were removed. For simulating machined notches at the edge and centre of the laminates, solid and cohesive elements were removed through the full thickness to represent a 1 mm wide notch. The notch lengths were defined based on the experimental fibre fracture widths determined for different

impact energies [24], where a typical edge notch model equivalent to the fibre fracture width due to an edge impact at 350 m/s is shown in *Figure 11*.

To impose the boundary conditions during the tensile tests, nodes through the thickness over a length of 50 mm from both ends were given Single Point Constraint (SPC) and Prescribed Motion boundary conditions in LS-DYNA. *Figure 12* illustrates the nodes used to implement the boundary conditions and their selection is a result of the coarse mesh outside the RoI. The selected nodes were allowed to translate in the 0° fibre direction and SPCs were applied to the other directions. A displacement degree of freedom was assigned to the selected nodes for the Prescribed Motion boundary condition. Furthermore, the densities of all materials were scaled up by three orders of magnitude to reduce the computational time and no significant dynamic effects were observed under quasi-static loading. Hourglass control (Type-6 in LS-DYNA) was used for all reduced-integration elements and it was ensured that the hourglass energy remained small compared to system internal energy.

5.2. Residual tensile strength comparison

The predicted tensile strength for edge-impacted and edge-notched laminates is illustrated in *Figure 13. Figure 14* provides the predicted results for centre-impacted and centre-notched laminates. The fibre fracture widths for centre impacts at 100 m/s and 150 m/s were not reported in [24] due to no fibre failure in the 0° plies and therefore, centre-notched simulations for the two lowest impact energies were not performed. Also shown in the plots are the experimental tensile results for the impacted laminates. For edge impacts, the predicted residual strengths differ from the experimental results by an average of 7%. For centre impacts, the predicted strengths vary from the experimental strength by an average difference of 16%. The differences observed between predicted and experimental strengths are due to the differences between predicted and experimental fibre fracture widths and the length of initial 0° splits, which will be discussed in the next section.

From *Figure 13*, the predicted strength of edge-notched laminates differs by an average of 9% from the experimental residual strength of edge-impacted laminates, except at 1.1 J, where the edge-notched laminate has a significantly lower strength than an edge-

impacted laminate. From *Figure 14*, the centre-notched laminates have similar strengths to centre-impacted laminates for intermediate impact energies (4.4 – 6.9 J). However, as the impact energy is increased, the residual strength of centre-notched laminates is unconservative in comparison to the experimental data for centre-impacted laminates due to the larger damage zones in the impacted laminates, which are accompanied by very large delamination areas [24] and longer 0° splits.

5.3. Propagation of initial 0° splits

To investigate the effects of splits, the fibre failure criterion was switched off in the model, allowing the damage development to be examined in terms of the growth of the initial 0° splits around the impact damage zone and at the notch tips. The edge-impacted and the edge-notched laminates corresponding to maximum impact energy of 13.5 J are considered here. The growth of 0° splits is analysed against the strain energy release rate, G. The strain energy release rate, G is calculated according to *Equation (3)* [34] which *i*s valid for quasi-isotropic laminates assuming propagation of sharp crack.

$$G = \frac{\pi C f^2 \sigma_g^2}{2E} \tag{3}$$

where $\sigma_g$is the applied gross section stress, f = 1.38 is a geometric parameter to account for the effect of finite width in the edge cases, C is the fibre fracture width and E = 61.6 GPa is the in-plane Young's modulus.

The split development in central double and single outboard 0° plies in an edge-impacted laminate and the equivalent edge-notched laminate are shown in *Figure 15*. As G is increased, the initial 0° splits in the impacted laminate show very small or negligible growth. In comparison, the initial 0° splits in the notched laminate grow with increasing G. At failure, the central double 0° plies have longer splits than the single outboard 0° plies. The equivalent Stress Concentration Factors (SCFs) in the 0° plies are also studied for the impacted and notched laminates. The maximum elemental stress in the 0° plies is divided by a factor of 2.61 to obtain an equivalent value for the laminate. This factor represents the ratio between the

stress in the 0° ply and the average stress in the laminate according to Classical Laminate Theory (CLT). The equivalent SCF is then calculated using the equivalent laminate stress divided by the applied gross section stress.

Figure 16 illustrates the relationship between the equivalent SCFs and the applied nominal stress in the central double and single outboard 0° plies for both impacted and notched laminates. The equivalent SCFs decrease with increasing applied stress in the notched laminate as the 0° splits grow with increasing G. In contrast, the equivalent SCFs slowly increase with applied stress in the impacted laminate as the 0° splits have restricted growth with increasing G. This is due to an increase in stresses at the crack tip since the growth of splits is quite limited with increase in applied stress. At failure, the central double 0° plies have a lower equivalent SCF than the single outboard 0° plies because the splits are longer in the central double 0° plies. Comparing the equivalent SCFs in notched and impacted laminates, they are initially different. As the load increases, they become closer and at failure, they are very similar. Hence, there is a good correlation between notched and impacted residual strength at most impact energies. Unlike edge notches, it is believed that significant differences in the equivalent SCFs at failure between centre-notched and centre-impacted laminates contribute to their less satisfactory correlation in residual tensile strength at most impact energies.

5.4. Damage zones comparison

The damage zones in notched specimens at 95% of the tensile failure load were analysed in [24]. The damage zone, D, is defined as the distance from the notch tip to the furthest 0° split in the test, whilst in the model, it is defined as the distance between the notch tip to the furthest fibre failure. The laminates corresponding to an impact energy of 13.5 J are considered in this section. While *Figure 17* illustrates the damage zones comparison in edge-notched laminates between the test and the model, *Figure 18* compares the experimental and predicted damage zones in centre-notched laminates. Overall, the predicted damage zones are in good agreement with the Computed Tomography (CT) scans at 95% of the failure load.

The damage zones in impacted laminates from the CT scans prior to tensile tests are then compared to the predicted damage zones in notched laminates at 95% of the failure load to further investigate the validity of the machined notch equivalence. The damage zone size in the edge-impacted specimen is 2.21 mm [24], which is 10% smaller than the predicted damage zone in an edge-notched laminate. The centre-impacted laminate shows a much larger damage zone size than the predicted damage zone size in the centre-notched laminate, differing by 58%. Large delamination areas in the centre-impacted laminates accompanied by more splitting contribute to the difference in damage zone sizes between centre-impacted and centre-notched laminates. In comparison to edge-impacted laminates, the large delamination areas in centre-impacted laminates at impact energy of 13.5 J are attributed to the high local interlaminar shear stresses arising due to greater rotational constraint at the impact point [24]. As a result, it is concluded that the machined notch equivalence to impact damage is valid for edge cases only.

6. Discussion

An average mesh size of 0.23 mm within the RoI has been used for all finite element models created. To analyse the mesh sensitivity of the results, the mesh size is almost halved to 0.11 mm within the RoI. For both edge and centre impacts, it was found that the fibre fracture widths were not significantly mesh sensitive. In terms of delamination area, there is negligible effect of mesh size as the impact energy is increased. For tensile simulations, FE models with 0.11 mm mesh size within the RoI are created to represent edge impact scenarios at 100 m/s and 350 m/s. For both impact cases considered, the fine mesh yields strength values which differ by an average of 3.5% in comparison to the baseline mesh. In order to minimise the computational time and to obtain an efficient finite element model, the baseline mesh size is considered adequate for this numerical study.

In this work, the surface of the projectile was aimed to strike the composite target. Changes in the projectile orientation were shown to significantly affect the extent of fibre failure, where the projectile oriented in a ‘point first’ configuration induced a larger extent of fibre failure due to its smaller contact area. The trend of increasing fibre damage as contact

area decreases agrees with the experimental study conducted by *Ulven et al.* [35], where the authors conducted ballistic perforation of carbon/epoxy composite panel with projectile geometries representing hemispherical, conical and flat tip. The cracking patterns in the samples were quantified and impact of conical projectile revealed the largest crack growth, followed by flat tip and hemispherical. While the projectile in this study has a mesh size of 0.1 mm and the laminate within the RoI has an average mesh size of 0.23 mm, there is a possibility that the effect of sharp contact in the 'Point' and 'Edge' configurations is not simulated as it should be. A finer mesh size for the projectile and the laminate represents a possible improvement, but computationally expensive.

For some impact energies, the impact model yielded smaller delamination areas than the experimental results. Since each ply is made up of one layer of single integration point elements, once it has delaminated either side, its bending stiffness is incorrect. Thus, if the laminate is separated into multiple layers of elements through the thickness and with fewer interface elements, the delamination area is expected to increase as the extent of delamination is dependent on the local bending stiffness of the discretised sub-laminate. *Schueler et al.* [33] obtained realistic results with a sub-laminate configuration where five interface layers were employed to simulate a 17-ply laminate. Therefore, an optimisation study on the number and position of interface layers needs to be carried out for better delamination area predictions. While the impact model consists of one element per ply, it is expected that increasing the through-thickness mesh density will lead to a more accurate load distribution and deformation throughout the model, but the run time costs would be significantly higher. It is expected that to obtain better delamination area predictions for the different impact configurations, each ply needs to be modelled with more than one solid element in the through-thickness direction.

For both edge and centre impacts, the differences between the predicted and experimental fibre fracture widths contribute to the differences between the predicted and experimental residual strengths. In addition, the propagation of initial 0° splits significantly affects the tensile failure stresses as longer splits blunt the stress concentrations. As the

residual tensile strength is mainly affected by the extent of fibre failure and the length of 0° splits, only edge notches have been shown to yield relatively close strength predictions to edge-impacted laminates and are therefore good equivalents.

7. Conclusions

The Hi-FEM modelling technique using cohesive interface elements provides a powerful tool for modelling different failure modes and their interactions under high velocity impact and quasi-static tensile events. High velocity oblique impacts were simulated, and the results were compared against experimental data. The trends for the extent of impact damage characterised in terms of fibre failure and delamination area were captured, although there were variations from the experimental results for some impact energies. At high velocities, changes in the projectile orientation before impact were shown to significantly influence the extent of fibre fracture. Further numerical analysis into the number of cohesive layers employed and decreasing the element size in the through thickness direction would be required to fully understand the implications on the predicted delamination area.

The predicted and experimental residual tensile strengths of impacted laminates were in good agreement for most impact energies. Edge-notched laminates were found to be a potential equivalent for tension after edge impact tests and the modelling gives further insight into the influence of the length and growth of initial 0° splits on the subsequent tensile failure stress. Simplified damage models with edge notches can provide good approximations, thus avoiding the high costs associated with intensive computational analysis of real impact damage.

Acknowledgements

The authors would like to acknowledge support from Rolls-Royce plc for this research through the Composites University Technology Centre (UTC) at the University of Bristol and from the Engineering and Physical Sciences Research Council (EPSRC) through the Centre for Doctoral Training in Advanced Composites at the University of Bristol (Grant no. EP/L016028/1).

Data availability

The data required to support the conclusions are provided in the results sections of this paper.

References

[1] Abrate S. Impact on laminated composites. Applied Mechanics Review Jan 1991;44(4),155-190.

[2] Cantwell WJ and Morton J. The impact resistance of composite materials – A review. Composites, 1991; 22(5):347-362.

[3] Cox B, Yang Q. In quest of virtual tests for structural composites. Science, 2006; 314:1102-1107.

[4] Abir MR, TayTE, Ridha M, Lee HP. Modelling damage growth in composites subjected to impact and compression after impact. Compos Struc, 2017; 168:13-25.

[5] Ebina M, Yoshimura A, Sakaue K, Waas AM. High fidelity simulation of low velocity impact behaviour of CFRP laminate. Comp Part A, 2018; 113:166-179.

[6] Cui H, Thomson D, Eskandari S, Petrinic N. A critical study on impact damage simulation of IM7/8552 composite laminate plate. Int J Impact Eng 2019; 127:100-109.

[7] Puck A, Schurmann H. Failure analysis of FRP laminates by means of physically based phenomenological models. Compos Sci Technol,2002; 58:30.

[8] Dávila CG, Camanho PP, Rose CA. Failure criteria for FRP laminates. J Compos Mater, 2005;39:323-345.

[9] Pernas-Sanchez J, Artero-Guerrero JA, Zahr Vinuela J, Varas D, Lopez-Puente J. Numerical analysis of high velocity impacts on unidirectional laminates. Comp Struc, 2014; 107: 629-634.

[10] Dugdale DS. Yielding of steel sheets containing slits. J Mech Phys Solids, 1960; 8(2):100-104.

[11] Camanho PP, Davila CG. Mixed-mode decohesion finite elements for the simulation of delamiantion in composite materials. NASA/TM-2002-211737, 2002;1:1-37.

[12] Xu X, Wisnom MR, Li X, Hallett SR. A numerical investigation into size effects in centre-notched quasi-isotropic carbon/epoxy laminates. J Comp Sci Technol, 2015; 111:32-39.

[13] Li X, Hallett SR, Wisnom MR. A finite element based statistical model for progressive tensile fibre failure in composite laminates. Comp Part B, 2013;45(1):433-439.

[14] Xu X, Wisnom Mr, Hallett SR. Deducing the R-curve for trans-laminar fracture from a virtual Over-height Compact Tension (OCT) test. Comp Part A, 2019; 118:-162-170.

[15] Li X, Hallett SR, Wisnom MR. Modelling the effect of gaps and overlaps in automated fibre placement (AFP) – manufactured laminates, Sci Eng Compos Matter, 2015;22(2): 115-129.

[16] ASTM D7137/D7137M-17. Standard test method for compressive residual strength properties of damaged polymer matrix composite plates, ASTM International, West Conshohocken, PA, 2017, www.astm.org

[17] Sun XC, Hallett SR. Failure mechanisms and damage evolution of laminated composites under compression after impact (CAI): experimental and numerical study. Comp Part A, 2018;104:41-59.

[18] Sanchez-Saez S, Barbero E, Zaera R, Navarro C. Compression after impact of thin composite laminates. Comp Sci Tech 2005;65(13):1911–9.

[19] Koo JM, Choi JH, Seok CS. Prediction of residual strength after impact of CFRP composite structures, International Journal of Precision Engineering and Manufacturing, 2017; 15: 1323-1329.

[20] Romano F, Di Caprio F, Mercurio U. Compression after impact analysis of composite panels and equivalent hole method. Procedia Eng 2016;167:182-189.

[21] Nettles AT. Notched compression strength of 18-ply laminates with various percentages of 0 plies. Compos Mater 2014;49(4):495-505.

[22] Puhui C, Zhen S, Junyang W. A new method for compression after impact strength prediction of composite laminates. Compost Mater 2002;36:589-610.

[23] Wallin M, Saarela O. Compression strength of notched and impact damaged composite laminates. In: Proceedings of 26th Congress of the International Council of the Aeronautical Sciences. Achorage, Alaska, USA, 14th – 19th Sept 2008.

[24] Kristnama AR, Xu X, Wisnom MR, Hallett SR, Nowell D. Experimental investigation of high velocity oblique impact and residual tensile strength of carbon/epoxy laminates. J Comp Sci Technol, 2019; 182:107772.

[25] Wisnom MR. Size effects in the testing of fibre-composite materials. J Comp Sci Technol, 1999; 59:1937–57.

[26] Wisnom MR, Khan B, Hallett SR. Size effects in unnotched tensile strength of unidirectional and quasi-isotropic carbon/epoxy composites. Comp Struc, 2008; 84:21–8.

[27] Li X, Hallett SR, Wisnom MR. Numerical investigation of progressive damage and the effect of layup in over-height compact tension tests. Comp Part A, 2012; 43:2137–50.

[28] HexTow® IM7 Carbon Fiber Datasheet, Hexcel®.

[29] Jiang W-G, Hallett SR, Green BG, Wisnom MR. A concise interface constitutive law for analysis of delamination and splitting in composite materials and its application to scaled notched tensile specimens. International J Numer Meth Eng, 2007; 69:1982–95.

[30] Li X, Hallett SR, Wisnom MR. Predicting the effect of through-thickness compressive stress on delamination using interface elements. Comp Part A, 2008;39:218-230.

[31] Czabaj MW, Ratcliffe JG. Comparison of intralaminar and interlaminar mode I fracture toughnesses of a unidirectional IM7/8552 carbon/epoxy composite, Compos Sci Technol,2013; 89:15-23.

[32] Yasaee M, Mohamed G, Pellegrino A, Petrinic N, Hallett SR. Strain rate dependence of mode II delamination resistance in through thickness reinforced laminated composites, Int J Impact Eng,2017; 107:1-11.

[33] Schueler D, Toso-Pentecote N, Voggenreiter H. Simulation of high velocity impact on composite structures – model implementation and validation. Applied Composite Materials, 2016; 23:857-878.

[34] Edwards HL, Wanhill RJH. Fracture mechanics: Edward Arnold, Delftse Uitgevers Maatchappij; 1984.

[35] Ulven C, Vaidya UK, Hosur MV. Effect of projectile shape during ballistic perforation of VARTM carbon/epoxy composite panels. Compos Struc, 2003;61:143-150.

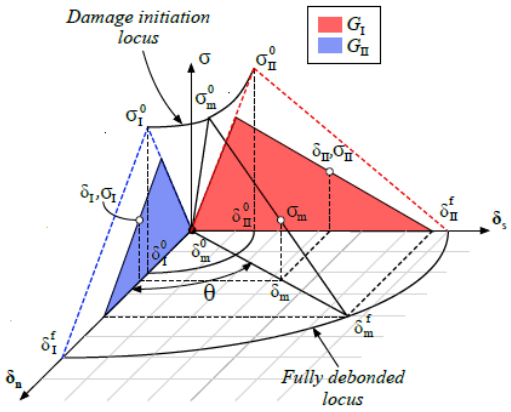

Figure 1: Traction-separation law of a cohesive element [12].

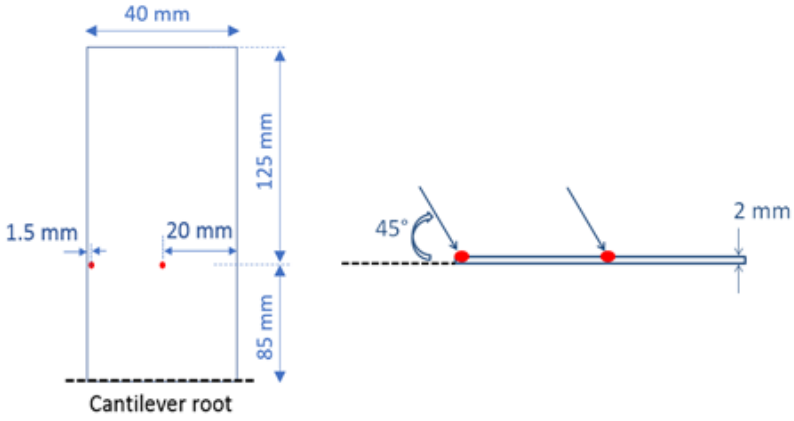

Figure 2: Impact positions shown by red dots on a laminate – image on the left showing the front view and image on the right illustrating the view from the root [24].

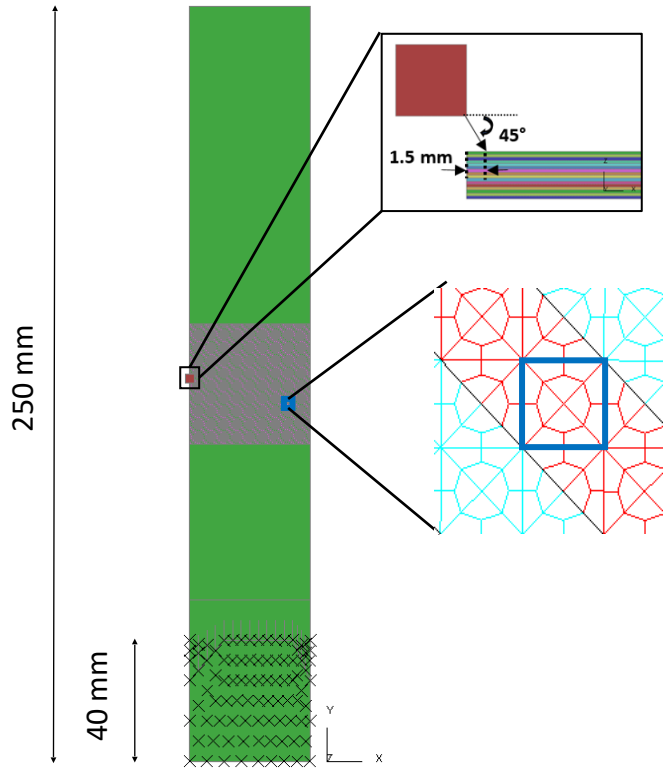

Figure 3: Laminate model showing boundary conditions applied to nodes marked as 'X'. The unit cell meshing technique applied to the Region of Interest (RoI) is also shown to the right and the orientation of the projectile before impact is shown on the top right.

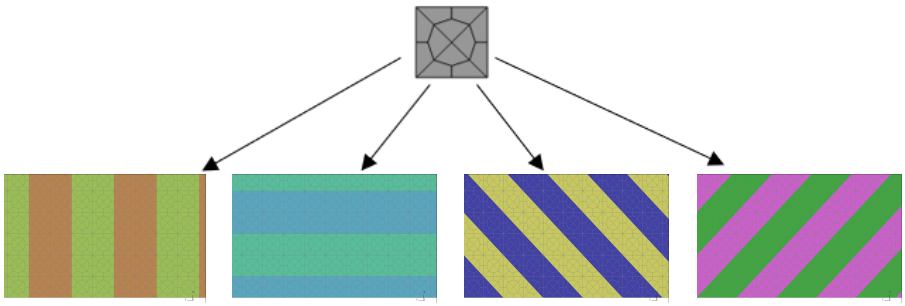

Figure 4: A unit cell pattern containing 12 solid elements (top) is repeated along the length and width of the specimen to create the mesh within the RoI. The colours following the crack orientation indicate the locations of cohesive elements in the 0°, 90°, 45° and -45° plies (bottom left to right).

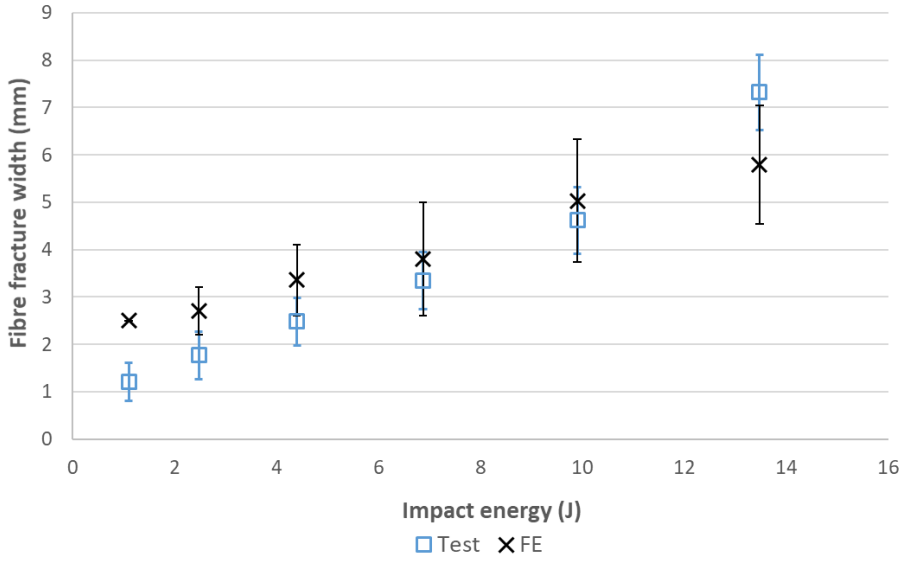

Figure 5: Fibre fracture widths for all edge-impacted laminates over a range of impact energies – Test [24] versus FE.

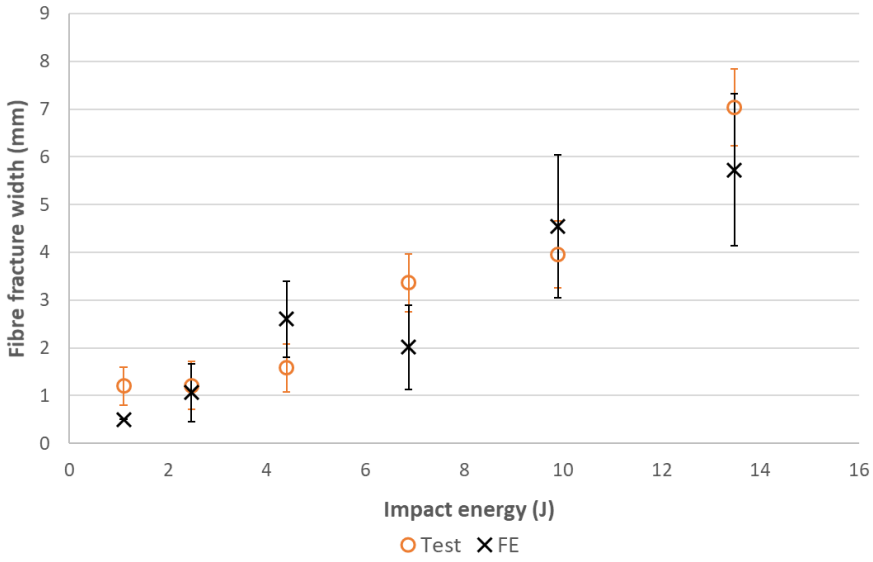

Figure 6: Fibre fracture widths for all centre-impacted laminates over a range of impact energies – Test [24] versus FE.

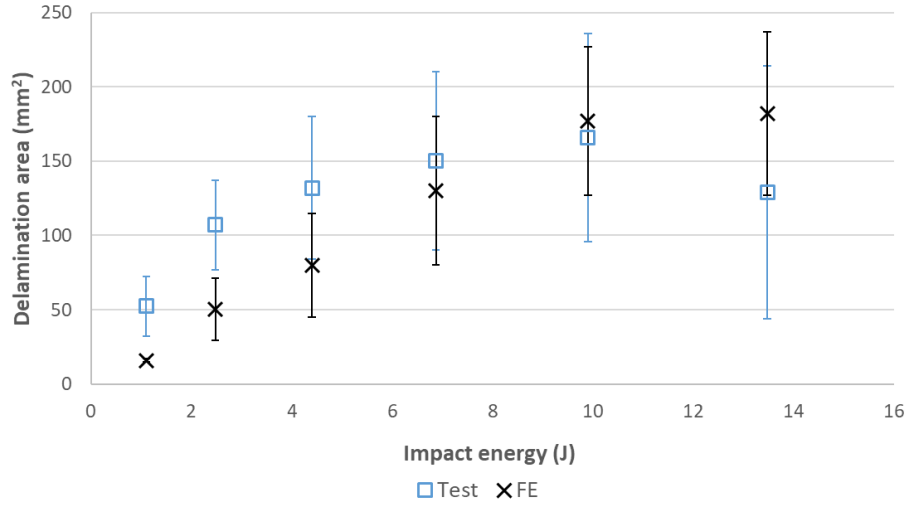

Figure 7: Delamination area for all edge- impacted laminates over a range of impact energies – Test [24] versus FE.

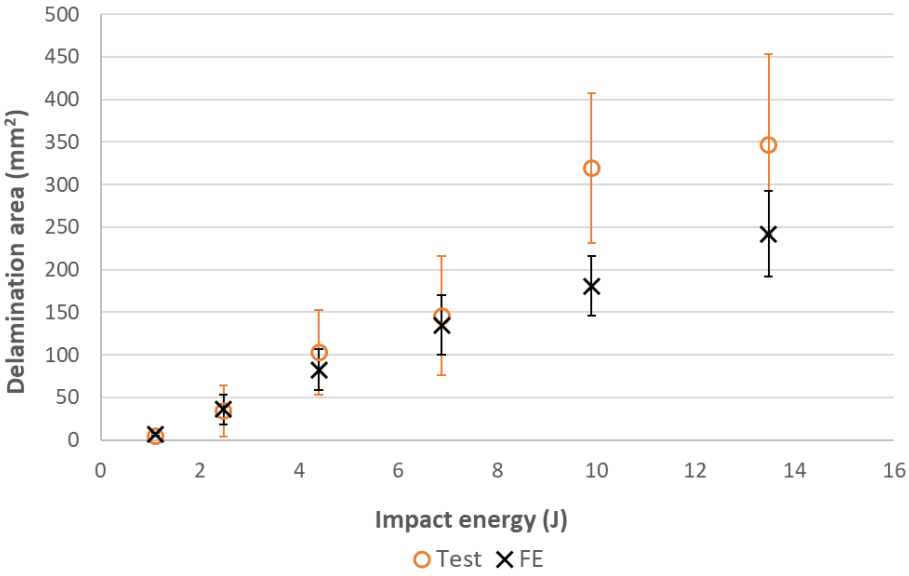

Figure 8: Delamination area for all centre-impacted laminates over a range of impact energies – Test [24] versus FE.

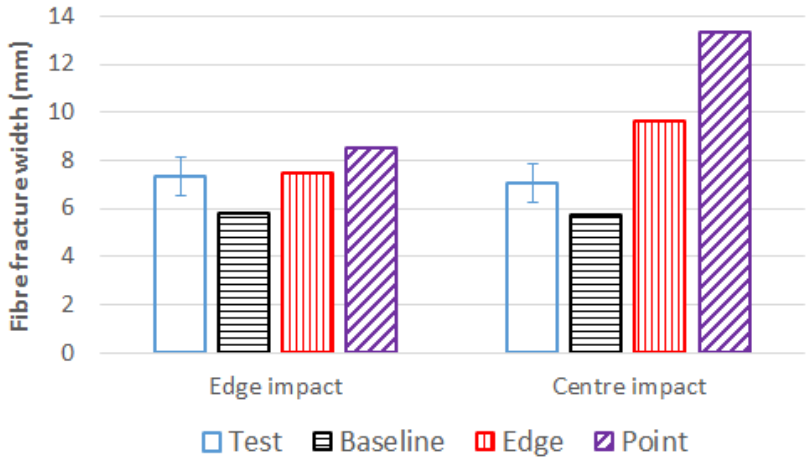

Figure 9: The variations in the extent of fibre fracture widths observed in edge- and centre-impacted laminates at 13.5 J for different projectile's orientations.

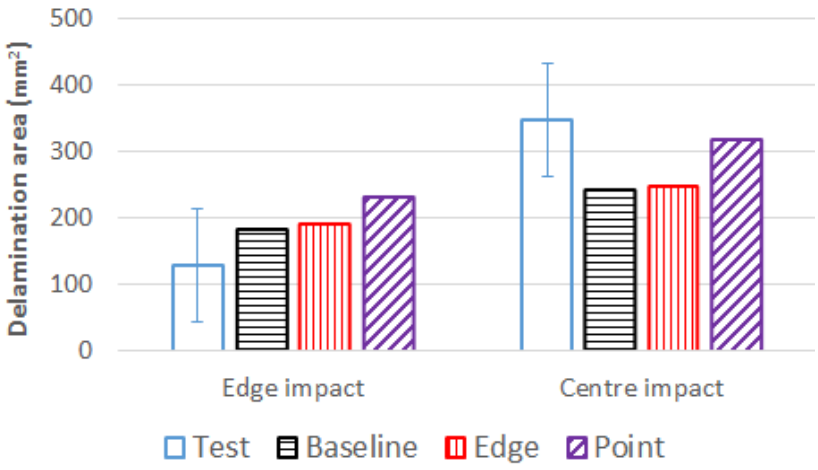

Figure 10: *The variations in the delamination areas observed in edge- and centre-impacted laminates at 13.5 J for different projectile's orientations.*

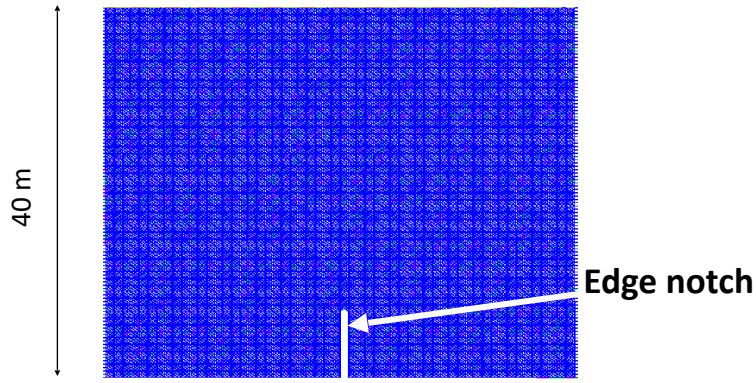

Figure 11: Machined notch representation within the RoI. Notch length is equivalent to fibre fracture width in edge-impacted laminate at 350 m/s, which is equal to 7.32 mm.

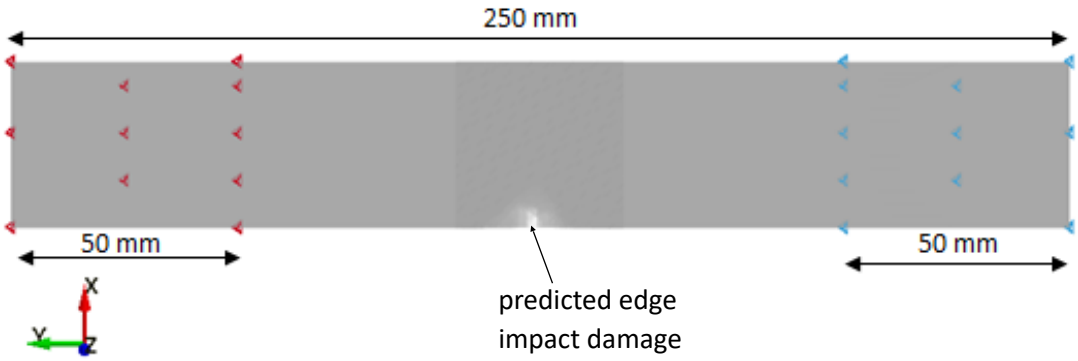

Figure 12: Selected nodes, denoted by triangular marks, are employed to define the boundary conditions for quasi-static tensile test simulation.

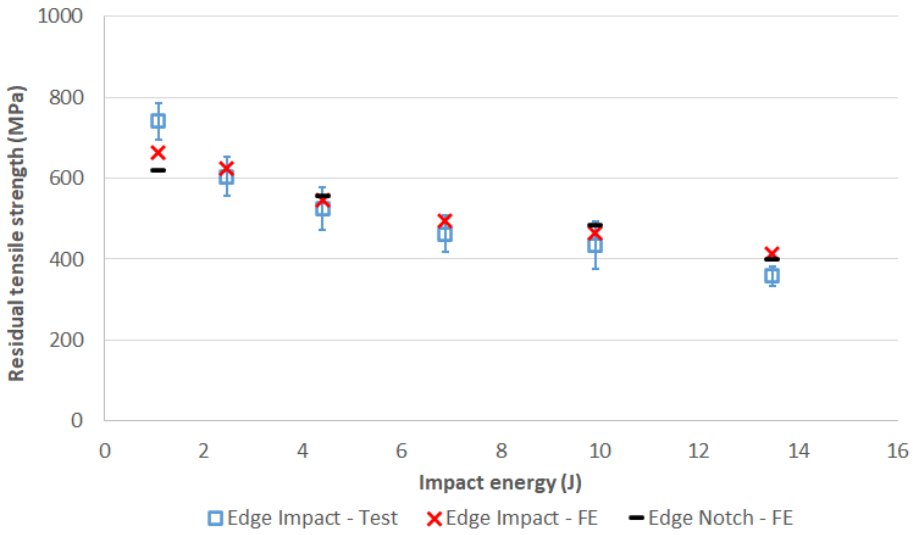

Figure 13: Residual tensile strength versus impact energy for edge-impacted laminates (Test [24] and FE) and edge-notched laminates (FE).

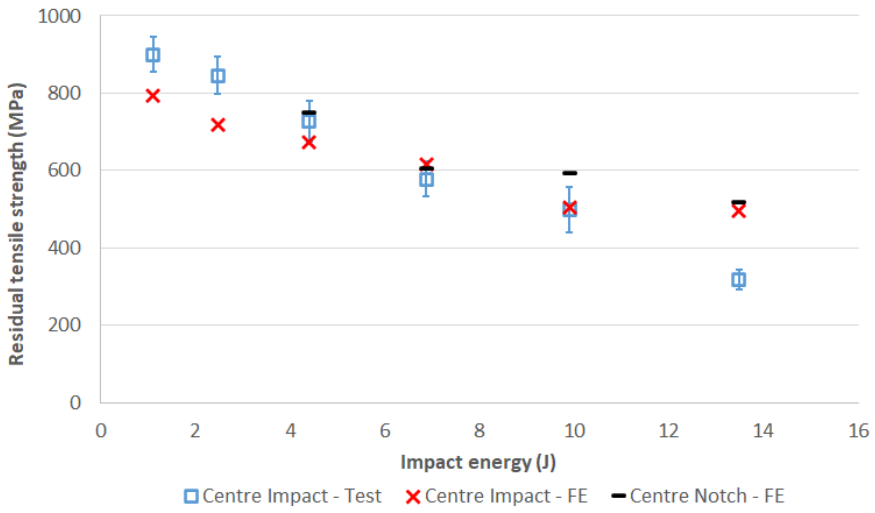

Figure 14: Residual tensile strength versus impact energy for centre-impacted laminates (Test [24] and FE) and centre-notched laminates (FE).

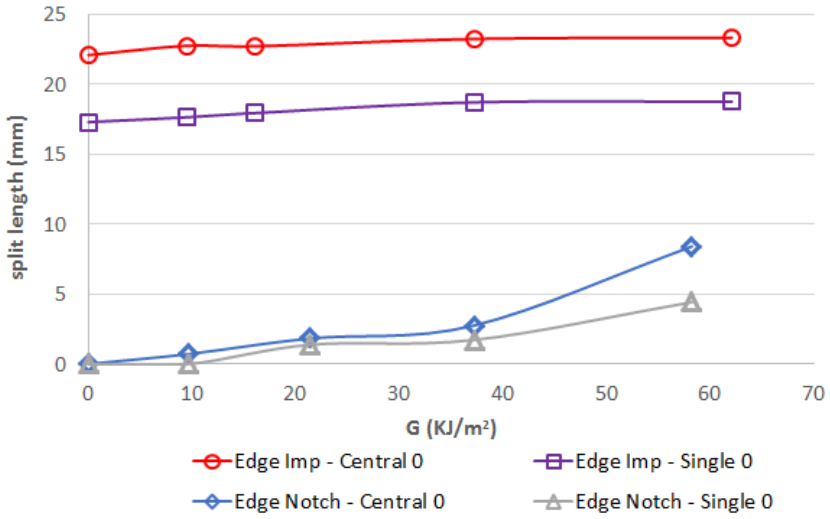

Figure 15: Development of the initial splits in the 0° plies for edge-impacted and edge-notched laminates at an impact energy of 13.5 J.

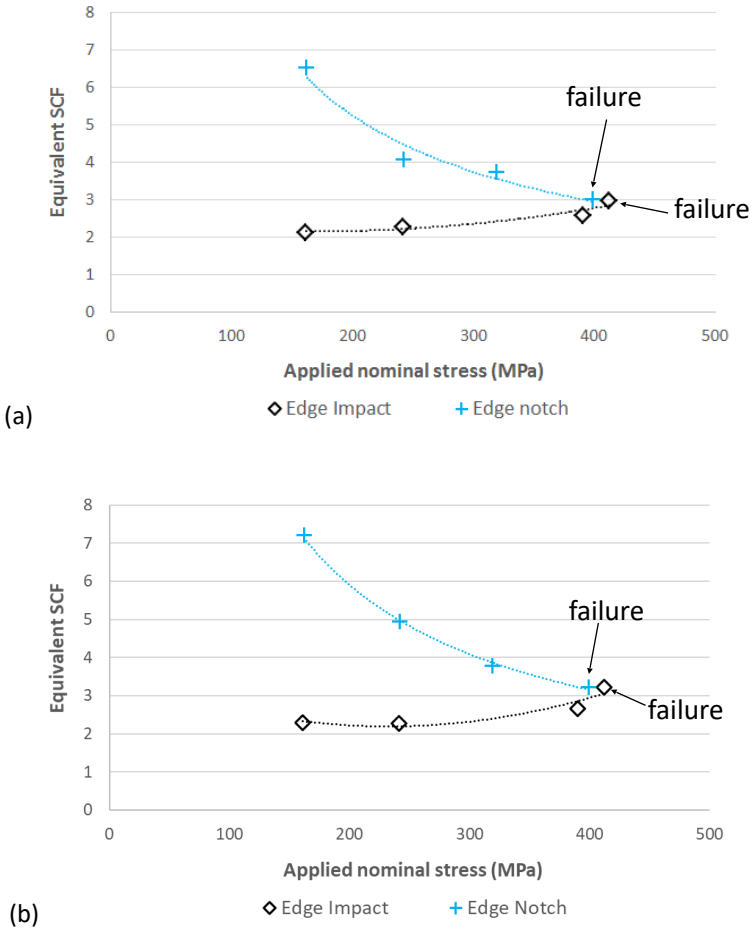

Figure 16: Development of equivalent SCFs in (a) central double and (b) single outboard 0° plies for edge-impacted and edge-notched laminates corresponding to impact energy of 13.5 J.

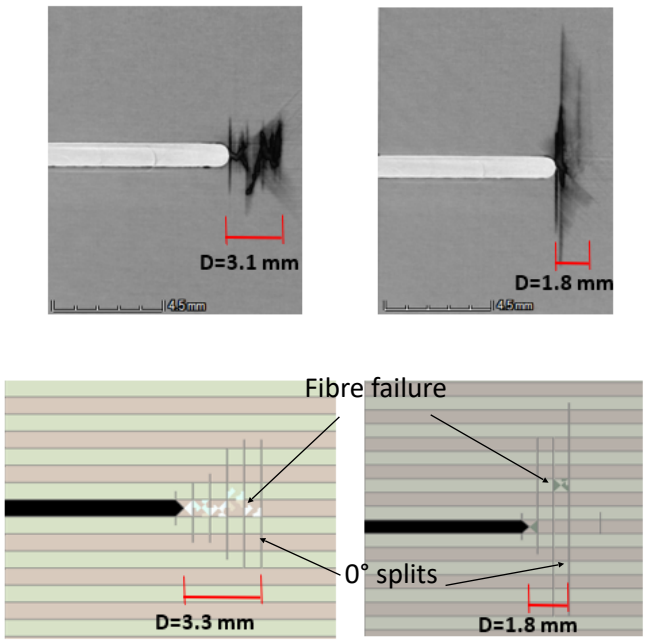

Figure 17: Damage zone, D, comparisons at 95% of the failure load in edge-notched laminates from single outboard 0° ply in test (top left) [24], central double 0° plies in test (top right) [24], single outboard 0° ply in model (bottom left) and double central 0° plies in model (bottom right).

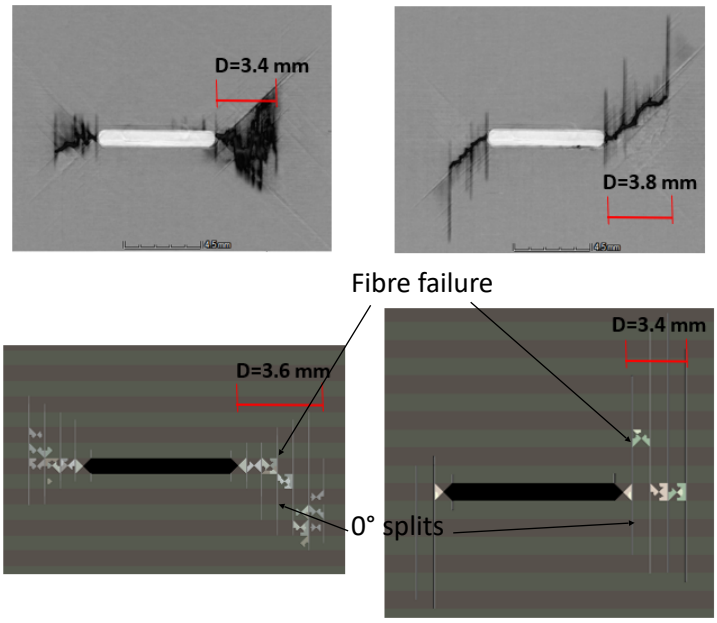

Figure 18: Damage zone comparisons at 95% of the failure load in centre-notched laminates from single outboard 0° ply in test (top left) [24] , central double 0° plies in test (top right) [24] , single outboard 0° ply in model (bottom left) and double central 0° plies in model (bottom right).

Table 1: Properties of lamina elements [12].

E_{11} (GPa)	$E_{22} = E_{33}$ (GPa)	$G_{12} = G_{13}$(GPa)	G_{23} (GPa)
161	11.4	5.17	3.98
$\alpha_{22} = \alpha_{33}$ ($°C^{-1}$)	α_{11} ($°C^{-1}$)	$\nu_{12}=\nu_{13}$	ν_{23}
$3x10^{-5}$	0.0	0.320	0.436

Table 2: Cohesive interface element properties [12,31,32].

G_{IC} (N/mm)	G_{IIC} (N/mm)	σ_{I}^{max} (MPa)	σ_{II}^{max} (MPa)
0.2[31]	0.9[32]	60[12]	90[12]